Check for updates

Received: 26 September 2023 | Revised: 22 February 2024 | Accepted: 23 March 2024

DOI: 10.1002/mrm.30109

RESEARCH ARTICLE

Magnetic Resonance in Medicine

Minimizing electric fields and increasing peripheral nerve stimulation thresholds using a body gradient array coil

Reza Babaloo[1,2] | **Ergin Atalar**[1,2]

[1]National Magnetic Resonance Research Center (UMRAM), Bilkent University, Ankara, Turkey

[2]Department of Electrical and Electronics Engineering, Bilkent University, Ankara, Turkey

Correspondence
Ergin Atalar, National Magnetic Resonance Research Center (UMRAM) & Department of Electrical and Electronics Engineering, Bilkent University, 06800, Bilkent, Ankara, Turkey.
Email: ergin.atalar@bilkent.edu.tr

Funding information
Türkiye Bilimsel ve Teknolojik Araştırma Kurumu, Grant/Award Number: 121E128; HORIZON EUROPE "MRITwins", Grant/Award Number: 101078393

Abstract

Purpose: To demonstrate the performance of gradient array coils in minimizing switched-gradient-induced electric fields (E-fields) and improving peripheral nerve stimulation (PNS) thresholds while generating gradient fields with adjustable linearity across customizable regions of linearity (ROLs).

Methods: A body gradient array coil is used to reduce the induced E-fields on the surface of a body model by modulating applied currents. This is achieved by performing an optimization problem with the peak E-field as the objective function and current amplitudes as unknown variables. Coil dimensions and winding patterns are fixed throughout the optimization, whereas other engineering metrics remain adjustable. Various scenarios are explored by manipulating adjustable parameters.

Results: The array design consistently yields lower E-fields and higher PNS thresholds across all scenarios compared with a conventional coil. When the gradient array coil generates target gradient fields within a 44-cm-diameter spherical ROL, the maximum E-field is reduced by 10%, 18%, and 61% for the X, Y, and Z gradients, respectively. Transitioning to a smaller ROL (24 cm) and relaxing the gradient linearity error results in further E-field reductions. In oblique gradients, the array coil demonstrates the most substantial reduction of 40% in the Z–Y direction. Among the investigated scenarios, the most significant increase of 4.3-fold is observed in the PNS thresholds.

Conclusion: Our study demonstrated that gradient array coils offer a promising pathway toward achieving high-performance gradient coils regarding gradient strength, slew rate, and PNS thresholds, especially in scenarios in which linear magnetic fields are required within specific target regions.

KEYWORDS

adjustable region of linearity, electromagnetic field simulation, flexible gradient linearity, gradient array coil, MRI safety, peripheral nerve stimulation

This is an open access article under the terms of the Creative Commons Attribution-NonCommercial License, which permits use, distribution and reproduction in any medium, provided the original work is properly cited and is not used for commercial purposes.

© 2024 The Authors. *Magnetic Resonance in Medicine* published by Wiley Periodicals LLC on behalf of International Society for Magnetic Resonance in Medicine.

1 | INTRODUCTION

Modern MRI scanners have a growing demand for gradient coils with strong gradient fields and fast switching capabilities.[1–5] These features are crucial to achieve better image quality and faster scan times. High gradient strength is essential for applications such as DWI. As the gradient strength increases, the duration of the diffusion gradient pulses decreases, leading to shorter TEs, an improved image SNR, and the potential for higher spatial resolution.[1] Moreover, a higher slew rate (SR) is desired, especially for techniques like EPI, to decrease the acquisition time.[6] Frequently used DWI sequences incorporate an EPI readout, and the simultaneous use of strong gradients and elevated slew rates leads to shortened TEs and echo spacings, increased SNR, and minimized motion artifacts, thereby enhancing the overall quality of the acquired images.[7–10]

Whole-body gradient coils typically have a maximum gradient strength (G_{max}) of less than 80 mT/m and a maximum SR no higher than 200 T/m/s. Because gradient coil inductance is proportional to the fifth power of coil radius,[11] pushing G_{max} beyond 80 mT/m would necessitate a considerable surge in peak power (e.g., 8 MVA/axis to achieve 300 mT/m).[1,12] Despite the advanced capabilities of such high-performance hardware, the simultaneous attainment of both high G_{max} and high SR has remained challenging due to physiological limitations imposed by peripheral nerve stimulation (PNS).[13–19] Rapid switching of strong magnetic fields (B-fields) induces electric fields (E-fields) within the human body, which can potentially trigger nerve stimulation. As a result, the use of high-performance gradient coils is markedly restricted by considerations of PNS rather than hardware limitations.

One of the crucial factors influencing the PNS thresholds of a given gradient coil is the size of region of linearity (ROL). In whole-body gradient coils with a large ROL, a large portion of the body is exposed to rapidly switching magnetic fields, leading to higher induced E-fields per unit slew rate. Several short-body and specialized head-insert gradient coils have been developed to enhance the performance of gradient coils without causing PNS. For instance, the compact 3T head-gradient coil[20] is capable of achieving a G_{max} of 80 and 700 T/m/s SR. The MAGNUS gradient coil[21] can simultaneously deliver 200 mT/m G_{max} and 500 T/m/s SR, and the recently introduced Impulse gradient coil[22] can achieve 200 mT/m G_{max} and 900 T/m/s SR. Because of their compact design and correspondingly smaller ROL, these advanced head gradient coils manage to minimize the exposure of the body to electromagnetic fields, which enables them to achieve high G_{max} and SR values without surpassing PNS thresholds. However, these specialized coils are designed exclusively for brain imaging applications, thus restricting their utility to other body parts.

Despite these efforts, PNS characteristics are assessed after the fabrication of the coil through experimental investigations conducted on healthy volunteers.[23–25] However, such studies provide only restricted insights into potential design modifications that could effectively mitigate PNS concerns. New gradient design algorithms have been proposed to incorporate constraints on the E-fields into the gradient coil design process, leading to PNS-optimized gradient coils. Davids et al.[26] introduced the PNS oracle, which uses a coupled model that integrates electromagnetic and neurodynamic aspects,[27,28] establishing a connection between the induced E-fields and the activation of peripheral nerves. Incorporating the PNS oracle into the gradient coil winding optimization process facilitates the swift evaluation of numerous potential coil designs, permitting the iterative refinement of these designs toward an optimal solution with higher PNS thresholds. Roemer et al.[29] developed a computationally efficient method to assess the spatial distribution of E-fields over homogeneous simplified body models. This method was subsequently incorporated into the gradient coil optimization algorithm to achieve a minimum E-field gradient coil design.[30]

Although these algorithms have succeeded in producing PNS-optimized gradient coil, they do not fully address two crucial challenges. First, specific engineering metrics such as the position, shape, and size of the ROL and the desired amount of field linearity in this region are considered fixed parameters during the gradient coil design process. However, the desired values of these parameters can change depending on the requirements of a particular application. Second, the PNS (or E-field) constraints are influenced by the dimensions of the body model under investigation and the specific scanning position used in the optimization process. For instance, PNS thresholds exhibit variations between male and female body models. During the design of a gradient coil, the size of the body is unknown; therefore, an average body model is used. Furthermore, a gradient coil design optimized for head imaging might yield lower thresholds for other scan landmarks not explicitly included in the coil winding optimization.[31] Modifying these parameters leads to a distinct design and coil winding, consequently affecting PNS thresholds.[17,26]

It has already been shown in the literature that incorporating additional coil elements[32,33] into the gradient coil configuration can effectively enhance gradient performance while mitigating PNS issues, even after the coil has been manufactured. Newly developed gradient array coils,[34–36] alternatively referred to as multicoil gradients[37] or matrix gradients,[38,9] offer an elevated level of flexibility, allowing for a higher degree of freedom in shaping

15222594, 2024, 3, Downloaded from https://onlinelibrary.wiley.com/doi/10.1002/mrm.30109 by Turkey Cochrane Evidence Aid, Wiley Online Library on [16/12/2024]. See the Terms and Conditions (https://onlinelibrary.wiley.com/terms-and-conditions) on Wiley Online Library for rules of use; OA articles are governed by the applicable Creative Commons License

magnetic field profiles. Array coils, consisting of multiple independently drivable channels, can generate target gradients with flexible linearity across a customizable ROL by optimizing the current amplitudes of the channels.

In this study, we use a whole-body gradient array coil, encompassing X, Y, and Z gradients along with their associated shields, to minimize the induced E-fields on the surface of a body model, thereby increasing PNS thresholds by modulating applied current levels to each of the channels. To accomplish this, we formulate an optimization problem with the maximum E-field magnitude ($|E|_{\max}$) as the objective function and the current amplitudes as the unknown parameters. The coil dimensions and winding patterns are fixed throughout the optimization process, whereas the other engineering metrics, such as ROL, gradient linearity, torque, magnetic field at the cryostat, and maximum applied current, remain adjustable. Various scenarios are explored by manipulating the adjustable parameters. Each scenario involves iterating through the optimization problem, yielding distinct combinations of currents that produce different E-fields and PNS thresholds. This approach enables a comprehensive exploration of the interplay between different parameters and their effect on the gradient coil performance and safety considerations, even after the coil has been manufactured. Some aspects of this work have already been presented as abstracts at the ISMRM conferences.[40,41]

2 | METHODS

2.1 | Body gradient array coil

The present study uses a whole-body gradient array coil encompassing X, Y, and Z gradients, including the primary gradient coils and their respective shielding coils. We adopt conventional coil windings of X and Y gradients, initially designed using the *Sim4Life* MRI gradient coil feature, to develop the gradient array coil. The *Sim4Life* gradient coil designer generates the required surface current density for a given coil geometry using the Boundary Element Method. The winding pattern is then extracted based on the chosen number of contours (loops) in the design process, assuming a thin wire model. The magnitude of the currents needed to drive the coil and generate a gradient field of a specified strength is attached to the windings. We specifically chose a high number of loops (376 loops for X and Y gradients) to ease the segmentation of the coils for the array design. Therefore, the resulting inductances of the conventional coils were relatively high (3.79 mH for X and 3.88 mH for Y) compared with common conventional gradient coils. A design with fewer loops, while maintaining the same surface current density, would indeed lead to coils with lower inductance. These conventional windings are divided into multiple channels, each of which can be independently driven with distinct current amplitudes when constructing an array configuration (Figure 1).

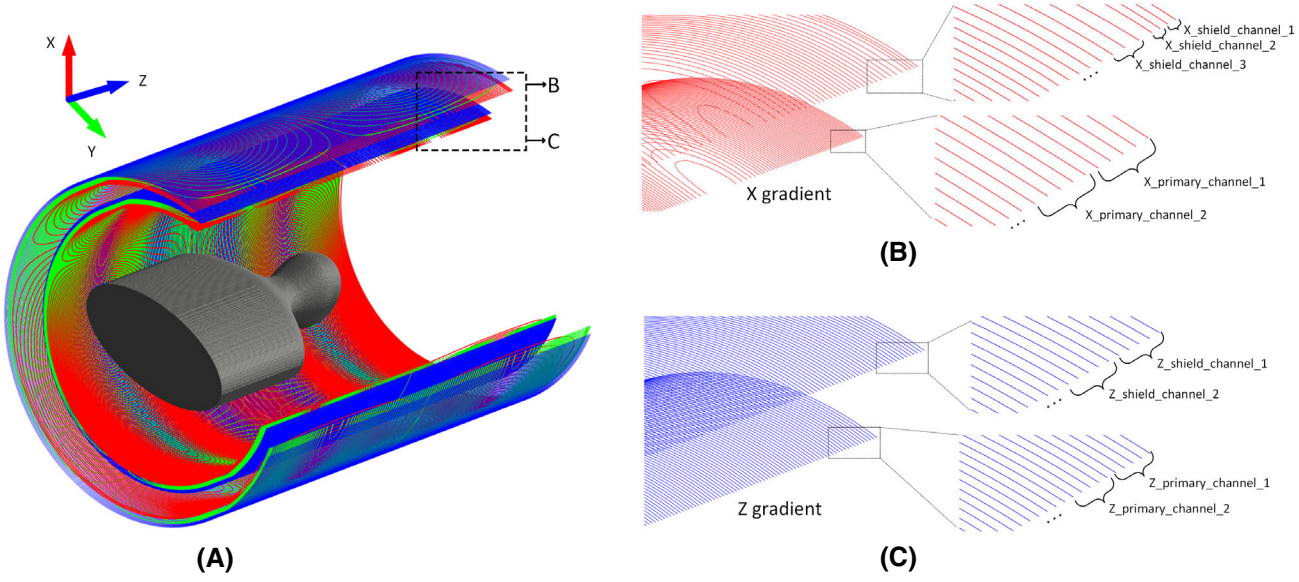

FIGURE 1 (A) Overall view of the body gradient array, including all three gradients (X, Y, and Z, both primary and shield coils) and the simplified body model. (B) Zoomed-in view of a portion of the X gradient. Each channel in the primary coil has five loops. In the shield coil, the first two channels of each quarter have two loops, whereas the remaining channels have three loops each. This figure does not show the arrangement of channels for the Y gradient, as it is similar to the X gradient. (C) Zoomed-in view of only a portion of the Z gradient. Each channel in the primary and shield coils has five loops.

15222594, 2024, 3, Downloaded from https://onlinelibrary.wiley.com/doi/10.1002/mrm.30109 by Turkey Cochrane Evidence Aid, Wiley Online Library on [16/12/2024]. See the Terms and Conditions (https://onlinelibrary.wiley.com/terms-and-conditions) on Wiley Online Library for rules of use; OA articles are governed by the applicable Creative Commons License

The number of channels is determined such that the total power consumption (volt × ampere) of all channels in the array design remains comparable to that of a conventional design (i.e., assuming m channels, the total power consumption of array design is $\sum_{k=1}^{m} V_k \times I_k$, where I_k is the current of kth channel and V_k is the required voltage to drive that channel); this value is similar to the total power consumption in all three coils (X, Y, and Z) of conventional gradients. Here, we consider a total of 96 channels, consisting of both primary and shield coils, for each directional gradient. The method for driving the mutually coupled gradient arrays has been previously detailed in prior publications.[34,42] It involves using the array coil inductance matrix, including self and mutual inductances, to compute the necessary voltages to drive the array channels and achieve the desired currents. The maximum self-inductance among the channels is 52 μH, and the maximum pairwise mutual inductance is 32 μH.

Figure 1B illustrates the configuration for the X gradient, where each quarter (out of eight quarters, four in primary and four in shield) is divided into 12 channels. In the primary coil, each channel accommodates five loops; however, in the shield coil, the first two channels of every quarter contain two loops, whereas the remaining channels have three loops each. The Y gradient follows the same arrangement as the X gradient. When equal currents are applied across all channels, the X and Y gradient arrays function as conventional gradient coils. For the Z gradient, the conventional design is replaced by uniformly distributed circular loops along the z-axis, covering the entire surface of the coil former as described in earlier publications.[34,35] Figure 1C depicts the Z gradient array configuration, consisting of 96 channels, each with five loops. It is important to note that while the winding pattern of the Z gradient array differs from that of a conventional Z gradient, it can still be programmed to operate as a conventional coil with typical functionality. The primary coil diameters for X, Y, and Z are 69 cm, 71 cm, and 73 cm, respectively, whereas the shield coil diameters for X, Y, and Z are 83 cm, 85 cm, and 87 cm, respectively. The length of the primary coils is 110 cm, and the shield coils have a length of 120 cm.

2.2 | Body model

In the current study, we adopt the same family of body models introduced in Roemer et al.[29] From this set of models representing the 2.5th, 50th, and 97.5th percentiles of both male and female adult populations, we selected the 50th percentile male model (Figure 1A). It has been previously established that PNS thresholds can be reliably predicted using such simplified body models. One advantage of using this simplified upper body model (rather than heterogeneous body models) is that the induced peak E-field occurs at the surface of the body model due to the uniform interior electrical properties. Consequently, only the surface sample points need to be considered, streamlining the computational calculations and significantly reducing the time required for optimization processes.

2.3 | Optimization problem

In conventional gradient coil design approaches (e.g., Boundary Element Method), a set of basis functions (stream functions) with a particular shape and unknown amplitude are optimized to determine the efficient coil winding pattern. In the context of array configurations, these basis functions take the form of an array of coils (channels) with a predefined winding pattern but unknown current amplitudes, represented by a vector $I = [i_1 \;\; i_2 \;\; \dots \;\; i_m]^T$, where m signifies the number of channels.

Before optimization (finding the optimal weight set I), a series of precomputations are conducted to assess the influence of each channel on various design metrics, such as B-fields, gradient fields, E-fields, and torques. This is achieved by applying a 1-kHz sinusoidal current waveform (1 A amplitude) to a specific channel while keeping the others at zero. For instance, the contribution of the gradient field (the spatial derivative of the magnetic field's z-component) to each sample point within the target region is calculated for every channel (basis). These contributions are then assembled into a matrix denoted as $\mathbf{G}$, in a way that the product of $\mathbf{G}I$ yields a description of the complete gradient field generated in the ROL. Subsequently, the E-field distributions corresponding to each channel are computed at the points located on the surface of the body model. As the E-field vectors generated by individual channels may vary in direction, separate matrices are constructed for each E-field component, namely $\mathbf{E}_x$, $\mathbf{E}_y$, and $\mathbf{E}_z$. The following equation is used to determine the overall E-fields at a given set of sample points:

$$E = (\mathbf{E}_x I)\hat{i} + \left(\mathbf{E}_y I\right)\hat{j} + (\mathbf{E}_z I)\hat{k} \tag{1}$$

We rely on low-frequency magneto quasi-static solvers provided by *Sim4Life* (Zurich Med Tech) for conducting field calculations in this study.

The optimization problem is formulated by determining current amplitudes that minimize the $|E|_{\max}$ on the surface of the body model while satisfying a set of constraints. The constraints are placed on the gradient linearity error at specific points across the target region (located on the surface of the ROL and the center point), the maximum tolerable magnetic field at the cryostat

15222594, 2024, 3, Downloaded from https://onlinelibrary.wiley.com/doi/10.1002/mrm.30109 by Turkey Cochrane Evidence Aid, Wiley Online Library on [16/12/2024]. See the Terms and Conditions (https://onlinelibrary.wiley.com/terms-and-conditions) on Wiley Online Library for rules of use; OA articles are governed by the applicable Creative Commons License

(a cylindrical shell in the z-direction with 92-cm diameter), the maximum current that the hardware can deliver, and considerations related to torque.

$$\begin{aligned} \min_{I} \quad & \max(|E|) \\ s.t. \quad & \left|\mathbf{G}I - g_{\text{target}}\right| \le \alpha \\ & \mathbf{G}_{\text{center}} I = g_{\text{target}} \\ & \left|\mathbf{B}_{\text{cryostat}} I\right| \le B_c \\ & |i_k| \le i_{\max} \quad \forall k = 1, \ldots, m \\ & \mathbf{T}I = 0 \end{aligned} \tag{2}$$

Where g_{target} denotes the vector of desired gradients at the specified sample points, and α represents the allowable peak gradient linearity error within the target ROL. Here, we specifically constrain the gradient field error, not the magnetic field (B_z) error, which allows the addition of uniform concomitant fields (B_x and B_y) for the X and Y gradient coils and a uniform B_z field for the Z coil. B_c is a threshold value that sets a limit on the magnetic field generated on the cryostat. This factor is crucial, as it accounts for the impact of eddy current effects. Although we define a threshold here, more advanced methodologies, such as those that calculate the total power dissipation within the cryostat, can also be implemented.[43] The torque constraint is specifically relevant for the X and Y gradient channels. When time-varying currents flow through them within a strong uniform magnetic field (B_0), they experience a rotational force that can lead to vibrations and instability in the system. The matrix **T** includes the torque of the assembly when a unit current is applied to the gradient channels within a unit uniform magnetic field.

The "fmincon" function from the *MATLAB* optimization toolbox is used to solve the optimization problem. This function is designed to locate a constrained minimum of a scalar function involving multiple variables, starting from an initial estimate. This process is commonly known as constrained nonlinear optimization or nonlinear programming. The final solution is a local minimum that meets the specified constraints. We use the interior-point algorithm with a random initial point, and the optimization procedure terminates when the objective function displays non-decreasing behavior in feasible directions. This function allows us to find an optimized solution that adheres to the constraints and minimizes the target objective function.

2.4 | Performance validation

The gradient array design introduces a range of distinctive features, including the ability to control the magnetic field profiles dynamically, adjust the shape and position of the ROL, and tailor gradient linearity according to the application's requirements. These features all contribute to the potential alteration of the induced E-fields, directly affecting the PNS thresholds.

To assess the efficacy of the gradient array in minimizing induced E-fields compared with the conventional coil, we explore four different scenarios. The first is a spherical ROL with 44-cm diameter. This is a standard mode of operation and the typical range of ROL for conventional body coils. Second is a spherical ROL with a smaller diameter (24 cm). Unlike conventional coils, the gradient array offers the flexibility to adjust the ROL size. This case is particularly suitable for dedicated body part imaging, such as head, cardiac, breast, or prostate imaging, where a smaller ROL is sufficient. However, it is crucial to note that merely reducing the imaging region in larger portions of the body (e.g., torso) might lead to artifacts and affect image quality. This potential issue can be assessed and addressed at the system design level, where it could influence sequence, coil, and reconstruction aspects. The gradient array design introduces flexibility in the gradient linearity, a parameter typically fixed in conventional designs and remains unchangeable after coil fabrication. In this scenario, we perform a sweep analysis of the gradient linearity error to demonstrate its influence on the induced E-fields. Third is a disk-shaped (slice) ROL. We consider circular disks in the z-direction (transverse slice, 2-cm thickness) at different positions as target linear regions, and the gradients are generated across all three spatial axes (X, Y, and Z). This example of dynamic ROL can be modified during a scanning session. The position and orientation of the disk can be adjusted in various directions. Finally, we consider oblique gradients within a 44-cm diameter spherical ROL. This case highlights the gradient array's versatility, indicating that it is not limited to the Cartesian directions.

In each of the outlined scenarios, the gradient array design can function comparably to the conventional coil in various aspects, including B-fields, target gradient strength, gradient linearity error, induced E-fields, and eddy currents. However, the practical aspects of constructing array coils pose challenges compared with conventional coils, such as dealing with input–output cabling, interconnects, insulation, and power dissipation from multiple channels. During the optimization process, we specifically define the target gradient strength, peak allowable gradient linearity error, and the maximum magnetic field at the cryostat to match the conventional coil performance. However, we retain flexibility in the other parameters. Our simulations use a target gradient strength of 40 mT/m. This particular value is chosen as an example for conducting the optimization process, and it can be adjusted by scaling the feeding current (output of the

15222594, 2024, 3, Downloaded from https://onlinelibrary.wiley.com/doi/10.1002/mrm.30109 by Turkey Cochrane Evidence Aid, Wiley Online Library on [16/12/2024]. See the Terms and Conditions (https://onlinelibrary.wiley.com/terms-and-conditions) on Wiley Online Library for rules of use; OA articles are governed by the applicable Creative Commons License

optimization) at a constant SR. The peak linearity errors for X, Y, and Z conventional gradient coils are 28%, 29%, and 23.75%, respectively. The same values are used to set the parameter α in the optimization. The peak gradient linearity error is computed from the coil's gradient field at all sample points and the target gradient via

$$\alpha = \frac{\max\left(\left|g_{\text{coil}} - g_{\text{target}}\right|\right)}{\max\left(\left|g_{\text{target}}\right|\right)} \tag{3}$$

The maximum magnetic fields generated at the cryostat by the X, Y, and Z conventional coils are 2.1 mT, 2.9 mT, and 1.1 mT, respectively, for the currents that generate 40 mT/m gradient strength. The same values are used to determine the parameter B_c within the optimization. It is essential to highlight that the induced E-fields depend on the gradient direction and the body position within the imaging volume. In our evaluation, we focus on positioning the head at the iso-center, individually examining all three spatial directions (x, y, and z) and combinations thereof.

Furthermore, we conduct calculations of PNS parameters for the four scenarios mentioned earlier to demonstrate the gradient array design's capability to increase PNS thresholds. According to the IEC 60601-2-33 safety standard,[44] one of the methods to determine PNS thresholds is computing PNS threshold parameters from the peak E-field on the surface of a uniform body model. This method relies on a principle known as the strength-duration relationship, which establishes a correlation between the minimum E-field required for a specified duration (Δt) to induce nerve stimulation. The key factors in this relationship are rheobase (rb), representing the minimum electric field needed to elicit nerve stimulation, and chronaxie (ch), representing the time constant for nerve stimulation. In accordance with the International Electrotechnical Commission's regulations,[44] rb is set to 2.2 V/m and ch to 360 μs for determining PNS thresholds from the E-fields produced by body gradient coils. Translating the E-field strength–duration relationship to a linear magneto-stimulation formula,[29] where PNS metrics are characterized by an intercept and slope, results in

$$\Delta G_{\text{stim}} = \Delta G_{\text{min}} + \Delta \text{t} \text{SR}_{\text{min}} \tag{4}$$

The PNS parameters ΔG_{min} and SR_{min} are the minimum gradient strength that induces stimulation at any switching time, and the minimum slew rate that causes stimulation at any gradient strength, respectively, and is given by[29]

$$\Delta G_{\text{min}} = \frac{\text{rb}}{|E|_{\text{max}}/\text{SR}}\text{ch}\ ,\ \ \text{SR}_{\text{min}} = \frac{\text{rb}}{|E|_{\text{max}}/\text{SR}} \tag{5}$$

where $|E|_{\text{max}}/\text{SR}$ is the maximum E-field magnitude per unit slew rate calculated on the body surface.

3 | RESULTS

Figure 2 illustrates the gradient field errors in the central and off-center planes as well as the magnitude of the E-fields on the surface of the body model for the conventional and array X gradients when the target field is generated within a 44-cm-diameter spherical ROL. This information is depicted for the Y and Z gradients in Figures 3 and 4, respectively. Although the contour plots of the gradient linearity error exhibit differences between the conventional and array coil designs, the peak gradient linearity error within the target ROL remains consistent for both configurations. The optimization procedure in the array coil design minimizes the induced E-fields by manipulating the B-field profiles while preserving the target gradient. The reduction in the $|E|_{\text{max}}$ for the X, Y, and Z gradients, as compared with the conventional coils, are 10%, 18%, and 61%, respectively.

The E-field reductions when using the X and Y gradients are not as substantial as the Z gradient, because the winding patterns of the X and Y gradient arrays are identical to the conventional designs. This particular design limits the extent of possible reductions in the E-fields. Moreover, the X and Y gradients necessitate torque balance, meaning that the E-fields cannot be further reduced without compromising this balance. Conversely, the significant reduction observed in the E-fields of the Z gradient can be attributed to the differences in its winding pattern from the conventional one. As such, the Z-gradient array offers more flexibility in minimizing E-fields.

Figure 5 compares the conventional and array coils' ability to generate the target gradient within a compact spherical ROL (24-cm diameter) with flexible gradient linearity error. The conventional coils demonstrate nearly perfect linear gradient fields inside this ROL (4% peak linearity error). The array coil can produce gradients that maintain the same peak linearity error while reducing induced E-fields. Although lower gradient linearity errors are preferable for imaging purposes, relaxing the constraint on peak gradient linearity error (α) during optimization can lead to even further reductions in the E-fields. Each green diamond in Figure 5 corresponds to a solution obtained from the optimization problem with a specific peak linearity error (up to 28%). For instance, by increasing the peak linearity error from 4% to 28% in the X gradient, it is possible to achieve a 38% reduction in the $|E|_{\text{max}}$ compared with the conventional X coil. Similarly, extending the acceptable peak linearity error from 4% to

15222594, 2024, 3, Downloaded from https://onlinelibrary.wiley.com/doi/10.1002/mrm.30109 by Turkey Cochrane Evidence Aid, Wiley Online Library on [16/12/2024]. See the Terms and Conditions (https://onlinelibrary.wiley.com/terms-and-conditions) on Wiley Online Library for rules of use; OA articles are governed by the applicable Creative Commons License

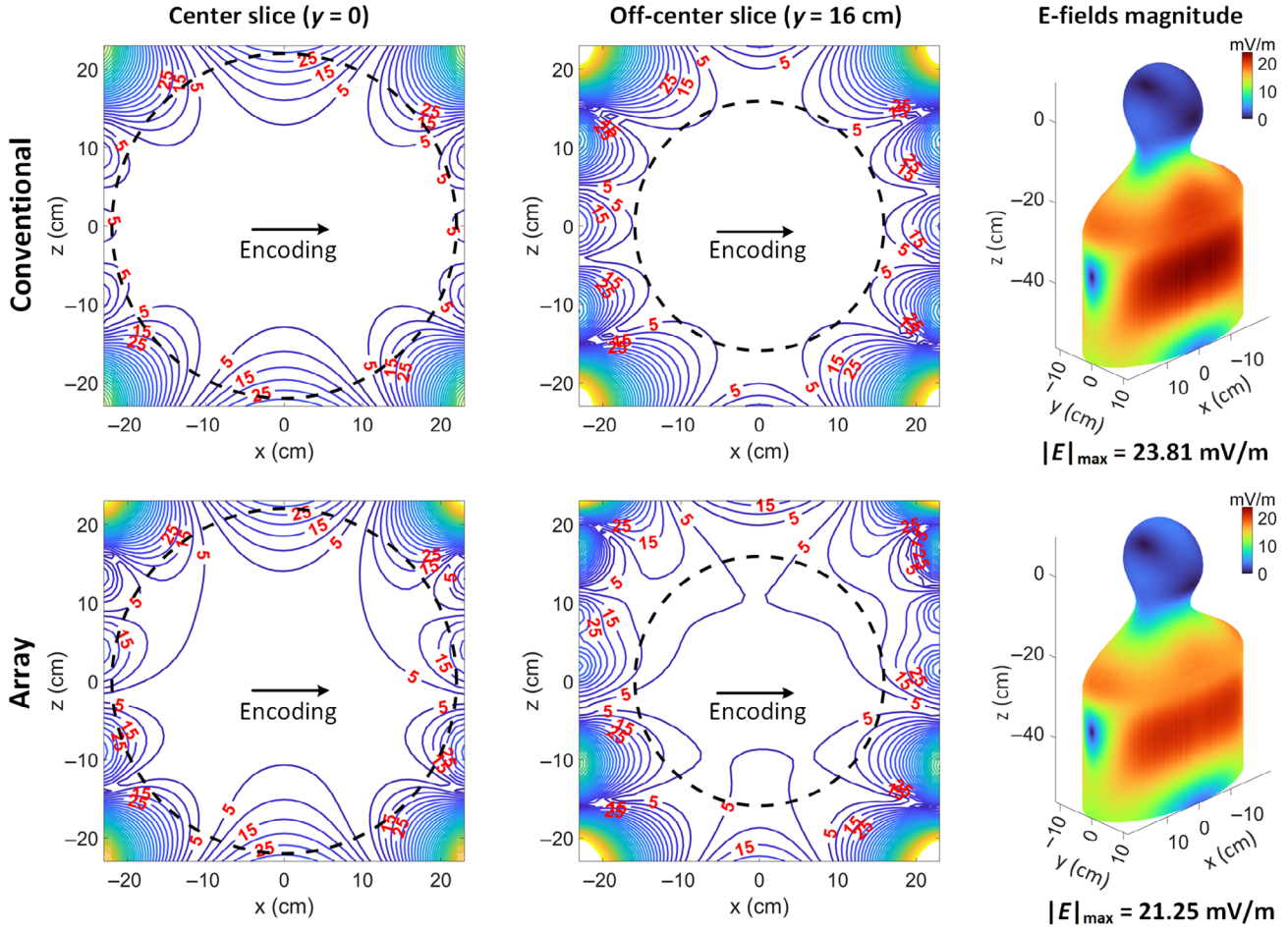

FIGURE 2 Performance comparison of the conventional and array coils while generating the target gradient in the x-direction within a 44-cm-diameter spherical region of linearity (ROL). The contour plots of the gradient linearity error (%), the normalized error between the induced and target gradient fields, are shown in center and off-center x-z planes. Although the overall pattern differs for the conventional and array coils, the peak gradient linearity error within the target ROL is identical (28%) for both designs. The magnitude of E-fields in units of mV/m for a unit slew rate of 1 T/m/s are shown for the conventional and array designs, with the array design exhibiting a 10% reduction in the $|E|_{max}$.

24% for the Z gradient leads to a remarkable reduction of 73% in the $|E|_{max}$.

Figure 6 illustrates the induced E-fields when the desired target gradient fields are generated within a circular disk in a transverse plane at three different positions, $z = 0$, $z = +6$ cm, and $z = -12$ cm. At the $z = 0$ position, the peak gradient linearity errors for X, Y, and Z gradients are 7%, 6%, and 1.7%, respectively. In this case, the $|E|_{max}$ experiences reductions of 25% for the X gradient, 17% for the Y gradient, and a significant 77% for the Z gradient. Shifting the disk to positive z results in lower E-fields due to reduced exposure of the body area to electromagnetic fields. Conversely, moving the disk to negative z increases the E-fields compared with the other two positions, as expected.

Figure 7 presents the E-field comparisons between the conventional and array coils when generating oblique gradients in different directions (X + Y, X + Z, and Z − Y) within a 44-cm-diameter spherical ROL. In all three oblique gradient directions examined, the induced E-fields through the array coil are notably lower than those associated with the conventional coil, even while maintaining the same peak linearity error. Specifically, the array coil demonstrates the most substantial reduction of 40% for $|E|_{max}$ in the Z−Y oblique gradient direction. For the X + Y and X + Z oblique gradient directions, the array coil achieves 17% and 39% reductions, respectively.

In Figure 8, the PNS curves corresponding to the different scenarios are presented. The PNS parameters are computed using Eqs. (4) and (5) to plot these curves. The dashed black line on the graph represents a hypothetical hardware limit, in this case, the human connectome gradient.[1] This figure illustrates that the array coil consistently yields higher PNS thresholds across all scenarios

15222594, 2024, 3, Downloaded from https://onlinelibrary.wiley.com/doi/10.1002/mrm.30109 by Turkey Cochrane Evidence Aid, Wiley Online Library on [16/12/2024]. See the Terms and Conditions (https://onlinelibrary.wiley.com/terms-and-conditions) on Wiley Online Library for rules of use; OA articles are governed by the applicable Creative Commons License

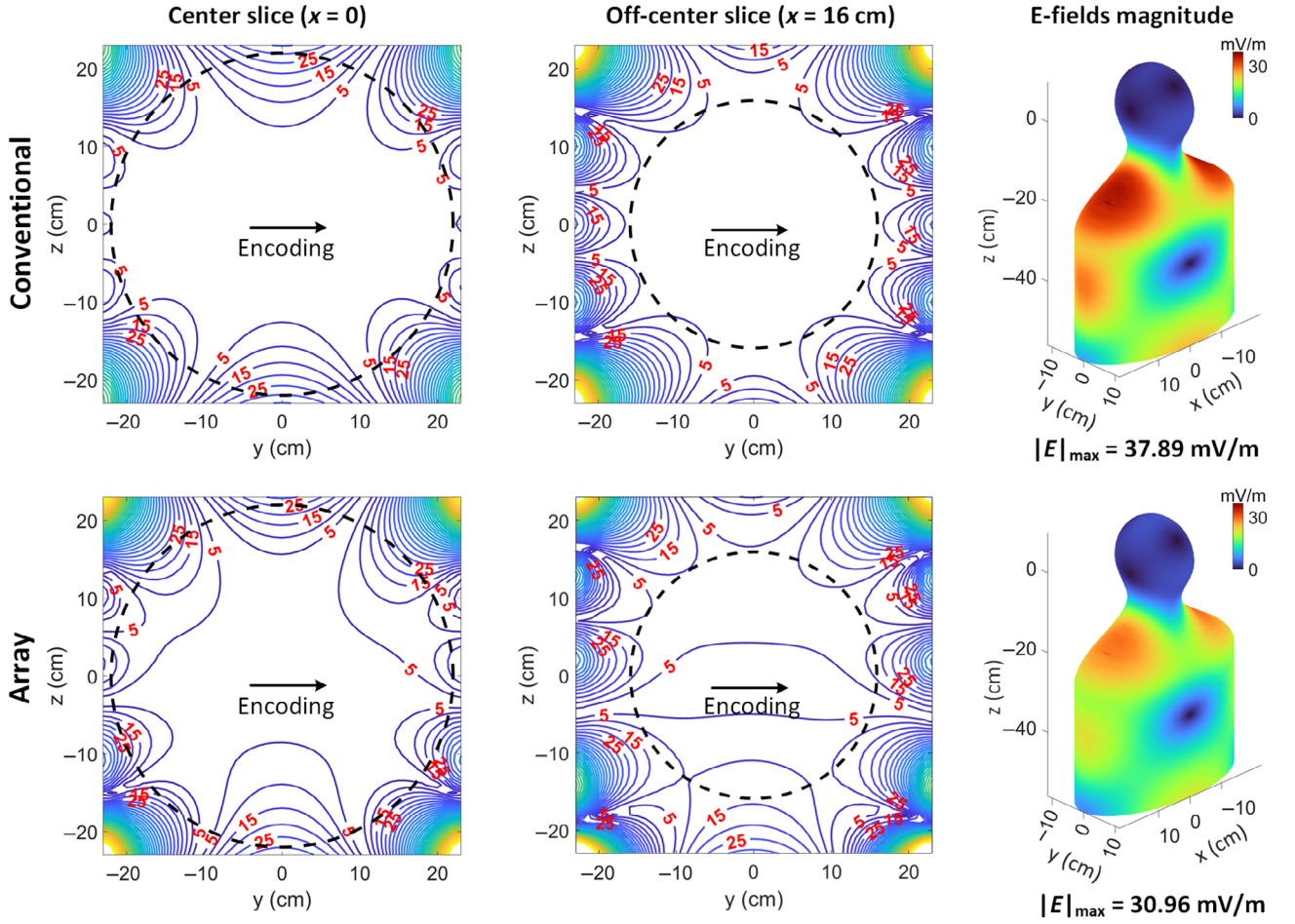

FIGURE 3 Performance comparison of the conventional and array coils while generating the target gradient in the y-direction within a 44-cm-diameter spherical region of linearity (ROL). The gradient linearity error (%) contour plots are shown in center and off-center y-z planes. Although the overall pattern differs between conventional and array coils, the peak gradient linearity error within the target ROL for both designs is the same (29%). The array design reduces the $|E|_{max}$ by 18% compared with the conventional one.

than the conventional coil. The increase in the PNS thresholds is particularly pronounced in the case of the Z gradient (2.7-fold for 44-cm ROL and 4.3-fold for disk ROL), where the array coil permits the use of the hardware's full performance without causing PNS. The summary of results, including the $|E|_{max}$ and PNS parameters (ΔG_{min} and SR_{min}), is provided in Table 1.

4 | DISCUSSION

In this study, we demonstrated the potential of a whole-body gradient coil designed in an array configuration to reduce induced E-fields on the surface of a simplified body model while producing a target gradient field with specific linearity error within a customizable ROL. Designing for minimal E-fields implies achieving higher gradient strengths and slew rates without surpassing PNS thresholds if the required hardware is available. Our results illustrated that the gradient array coil not only operates on par with the conventional coil but outperforms it in performance across different scenarios.

It is crucial to emphasize that our study does not aim to design a gradient array coil from the ground up. Parameters such as coil dimensions, X and Y coil winding patterns, shielding performance, and power consumption were selected in a manner similar to a conventional gradient coil (designed via *Sim4Life* software). Specifically, we did not modify the winding pattern of X and Y gradients to illustrate that driving even an existing conventional winding in the array mode can achieve better performance in terms of PNS thresholds. However, it is also possible to consider the other multicoil designs, like matrix gradient,[39] and compare their induced E-fields to the conventional coils, which is left for future investigations. We anticipate that by applying advanced gradient design techniques, it is possible to achieve further reductions in the induced E-fields.

15222594, 2024, 3, Downloaded from https://onlinelibrary.wiley.com/doi/10.1002/mrm.30109 by Turkey Cochrane Evidence Aid, Wiley Online Library on [16/12/2024]. See the Terms and Conditions (https://onlinelibrary.wiley.com/terms-and-conditions) on Wiley Online Library for rules of use; OA articles are governed by the applicable Creative Commons License

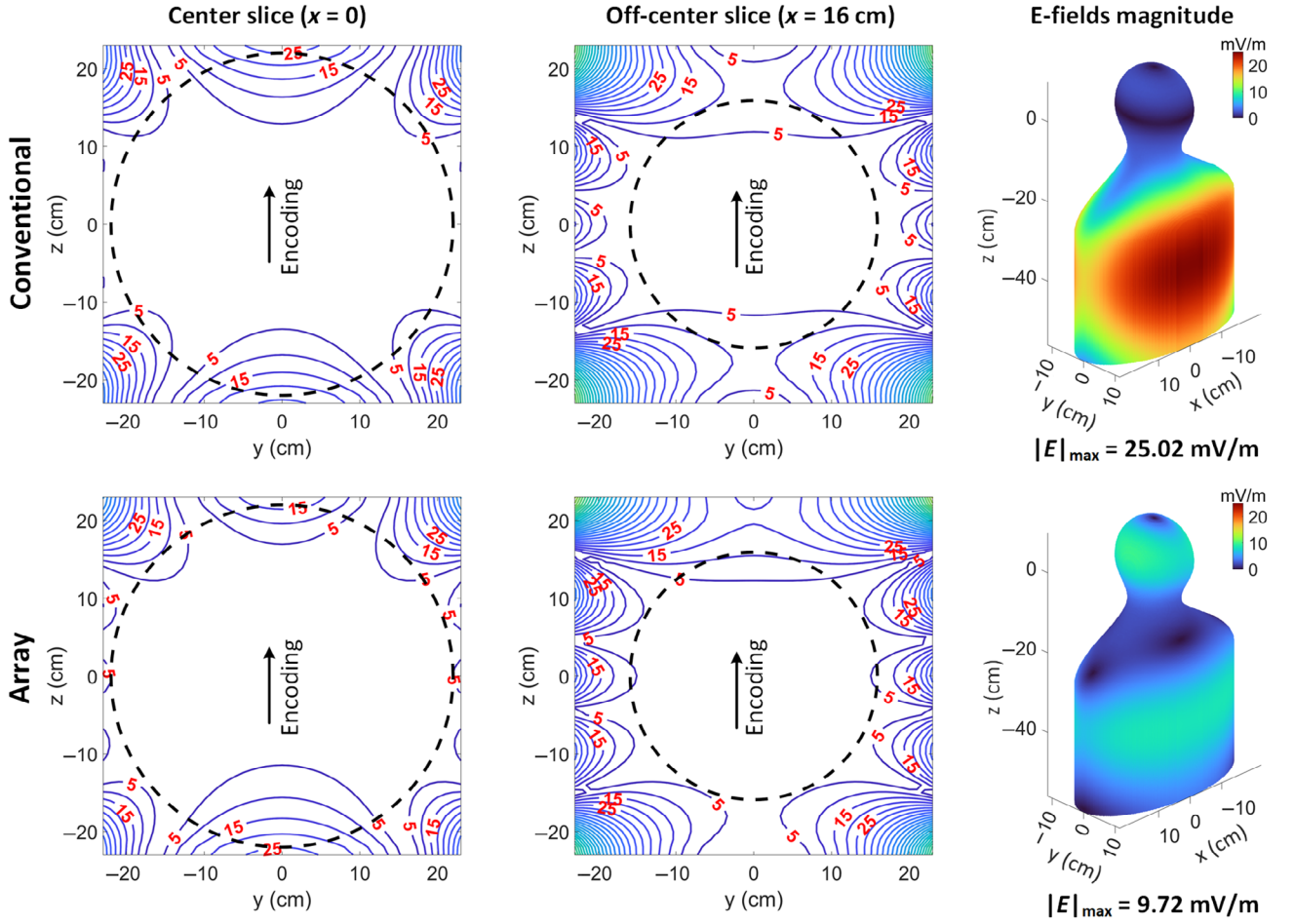

FIGURE 4 Performance comparison of the conventional and array coils while generating the target gradient in the z-direction within a 44-cm-diameter spherical region of linearity (ROL). The contour plots displaying the gradient linearity error (%) are presented in the center and off-center y-z planes. Although there are variations in the overall patterns between the conventional and array coils, the peak gradient linearity error within the target ROL for both designs is the same (23.75%). For the Z gradient, the array design exhibits a remarkable 61% reduction in the $|E|_{max}$ compared with the conventional design.

Engineering metrics like ROL size and allowable gradient linearity error are often dynamic and vary depending on the specific imaging requirements of each scan. The array design allows for the optimization of currents tailored to a specific application, enabling the generation of gradients suitable for that application. In head imaging applications, for example, the gradients within a large ROL (44-cm diameter) are no longer required. Optimizing the feeding currents to produce the required gradient within a smaller ROL (24-cm diameter) reduces the induced E-fields, as demonstrated in Figure 5. The array coil can minimize unnecessary exposure, reduce induced E-fields, and improve performance during imaging by customizing the ROL to a specific region.

Additionally, the acceptable linearity error in the array design can be adjusted as needed. For instance, by relaxing the peak linearity error, as depicted in our simulations, substantial reductions in the $|E|_{max}$ can be achieved (Figure 5). In the case of generating gradients within a disk-shaped ROL (ideal for applications like DWI), the gradient array coil demonstrated an impressive 77% reduction of the $|E|_{max}$ for the Z gradient compared with the conventional coil (Figure 6).

In the optimization, we focused on the gradient fields rather than magnetic fields, because the gradient of the magnetic fields primarily influences the spatial encoding in MRI. In conventional gradient coils, the magnetic field is typically zero at the origin, and higher magnetic fields are required toward the edges of the ROL to achieve the target gradient. Therefore, some body parts (chest and lower body) experience increased exposure to magnetic fields, leading to higher induced E-fields. The gradient array coil effectively reduces the E-fields by manipulating the magnetic field profiles while preserving the desired gradient. This manipulation can involve introducing uniform magnetic fields, such as having a nonzero magnetic field at

15222594, 2024, 3, Downloaded from https://onlinelibrary.wiley.com/doi/10.1002/mrm.30109 by Turkey Cochrane Evidence Aid, Wiley Online Library on [16/12/2024]. See the Terms and Conditions (https://onlinelibrary.wiley.com/terms-and-conditions) on Wiley Online Library for rules of use; OA articles are governed by the applicable Creative Commons License

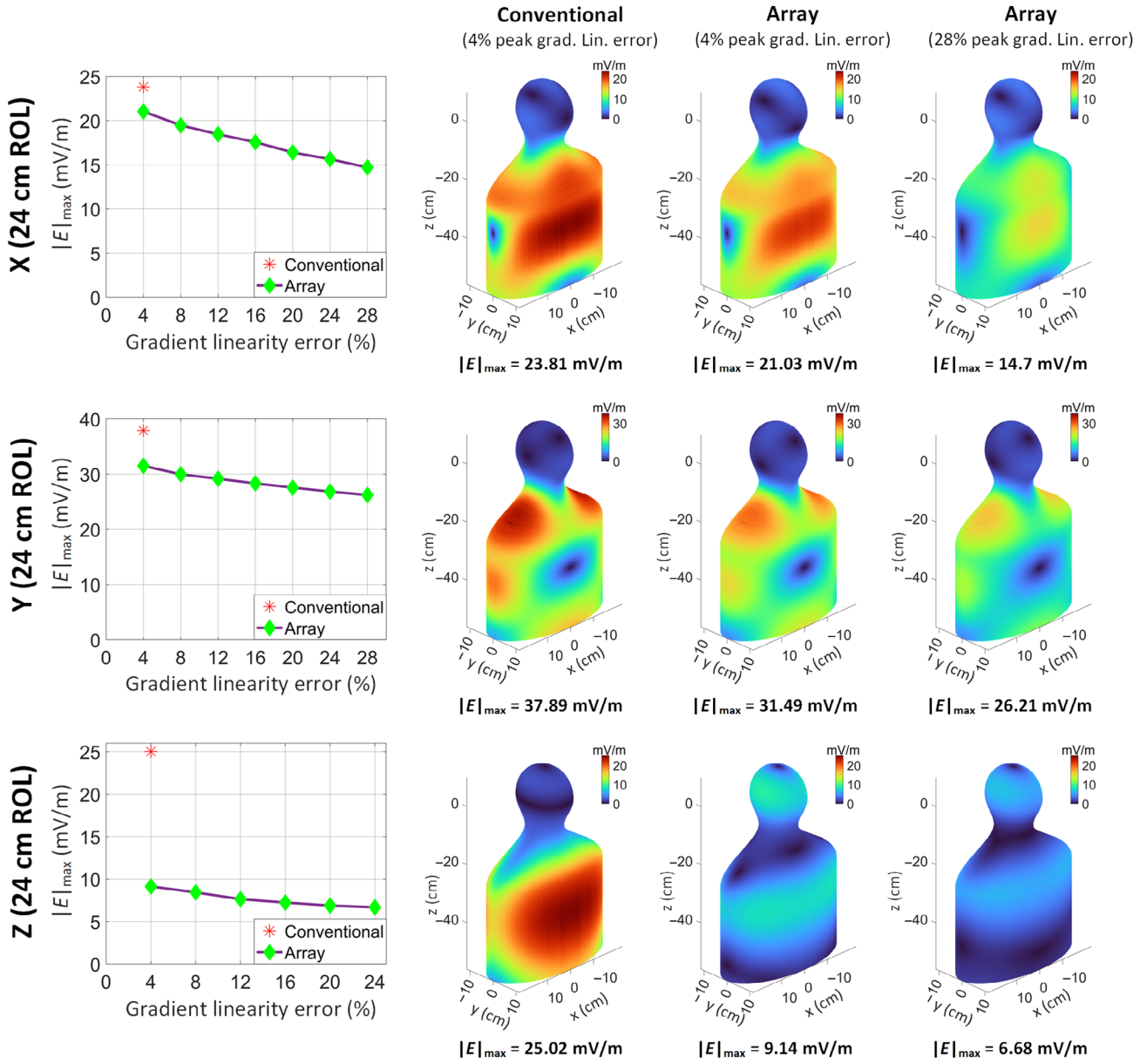

FIGURE 5 The E-field results for 24-cm-diameter spherical region of linearity (ROL). The induced E-fields for two different peak gradient linearity errors is shown. On the plots in the right column, each green diamond represents an optimization problem solution with a particular peak linearity error (up to 28%). The $|E|_{max}$ is reduced by allowing higher linearity error within the target ROL. For example, extending the acceptable peak linearity error from 4% to 28% for the X and Y gradients reduces the $|E|_{max}$ by 38% and 31%, respectively. Furthermore, increasing the peak linearity error from 4% to 24% in the Z gradient substantially reduces the E-fields by 73%. The E-field distributions on the surface of the body model are shown for different cases. Note that E-field color scales differ for the X, Y, and Z gradients.

the origin. The X and Y arrays primarily contribute uniform fields in B_x and B_y components (concomitant fields); however, the Z array introduces a uniform B_z field, which affects the NMR signal in the imaging region. However, this effect primarily manifests as a spatially uniform frequency shift, which can be addressed through RF modulation and basic signal processing methods. The B-field profiles of some cases are provided in Figure S1.

Considering a non-zero B_z at the center in array configuration may prompt a discussion that a conventional coil could also be designed with a non-zero B_z at the center and incorporate uniform fields in the design process.[33] This could potentially yield comparable results in reducing E-fields as observed in the array design (44-cm ROL). However, the advantage of the array lies in the flexibility of ROL shape and linearity error adjustment even after coil fabrication, affecting the induced E-fields. Using the array configuration eliminates the necessity to construct multiple coils for different applications. The current weightings of the array coil can be optimized offline for various

15222594, 2024, 3, Downloaded from https://onlinelibrary.wiley.com/doi/10.1002/mrm.30109 by Turkey Cochrane Evidence Aid, Wiley Online Library on [16/12/2024]. See the Terms and Conditions (https://onlinelibrary.wiley.com/terms-and-conditions) on Wiley Online Library for rules of use; OA articles are governed by the applicable Creative Commons License

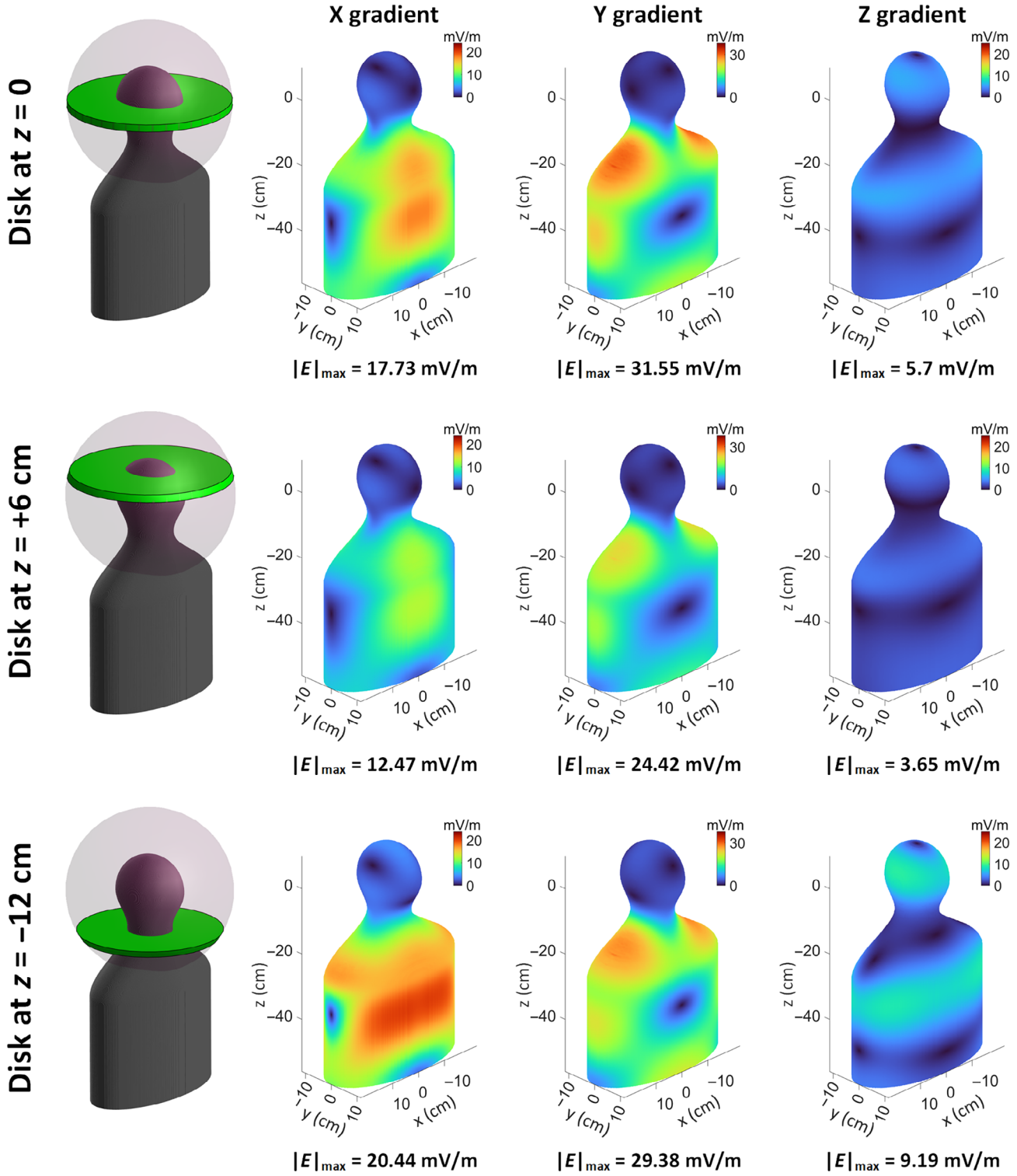

FIGURE 6 E-field distributions of the array coil when generating the gradients within a circular disk (2-cm thickness) in the transverse plane at $z = 0$, $z = +6$ cm, and $z = -12$ cm. For the disk at $z = 0$, the $|E|_{max}$ is reduced by 25%, 17%, and 77% for the X, Y, and Z gradients, respectively.

applications, and the resulting current combinations can be stored as lookup tables. Users can then conveniently select the operation mode based on specific application requirements. This flexibility underscores the adaptability and versatility of the array coil design.

In the context of gradient array design, providing coil performance per unit current becomes complicated due to the absence of a single current. In this case, the RMS of currents can be used to report such information. However, because different scenarios lead to different current

15222594, 2024, 3, Downloaded from https://onlinelibrary.wiley.com/doi/10.1002/mrm.30109 by Turkey Cochrane Evidence Aid, Wiley Online Library on [16/12/2024]. See the Terms and Conditions (https://onlinelibrary.wiley.com/terms-and-conditions) on Wiley Online Library for rules of use; OA articles are governed by the applicable Creative Commons License

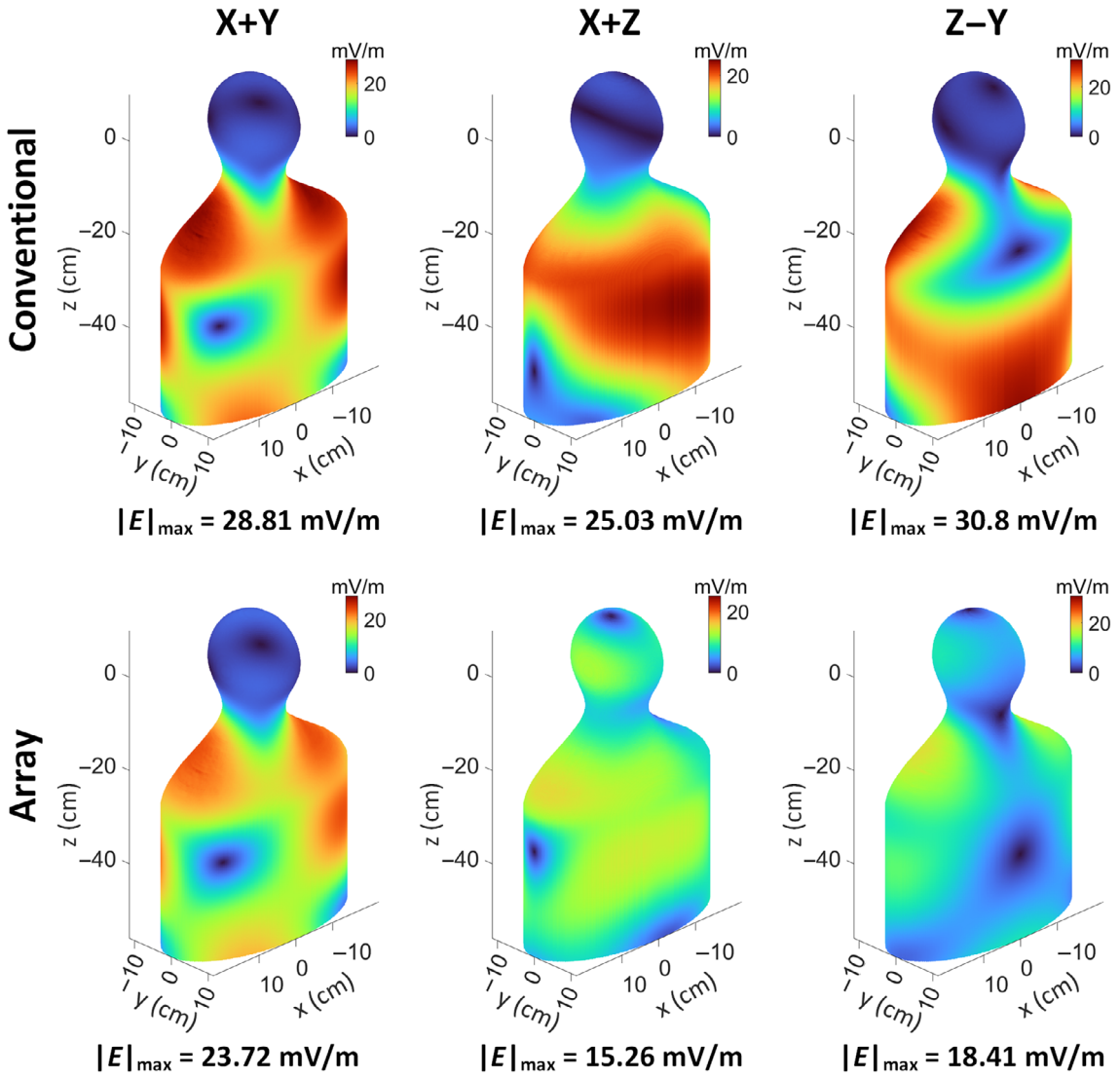

FIGURE 7 The comparison of E-filed distributions for the conventional and array coils when producing the oblique gradients within a 44-cm-diameter spherical region of linearity. Three different directions are evaluated: X + Y, X + Z, and Z − Y. The array coil demonstrates the most substantial reduction of 40% for $|E|_{max}$ in the Z − Y oblique gradient direction.

RMS values, providing a single performance value that is not applicable. For example, the field efficiency for the conventional X coil is 0.16 mT/m/A. However, for the X array coil in the 44-cm ROL case, the field efficiency is 0.14 mT/m/A_{rms}, and for the 24-cm ROL case (28% peak linearity error), it is 0.17 mT/m/A_{rms}. A similar method can be used to report the shielding performance. For instance, the shielding performance of the conventional X coil is 8.75 μT/A; again, for the array mode with a 44-cm ROL, it is 7.36 μT/A_{rms}; and for the 24-cm ROL, it is 8.9 μT/A_{rms}. The current amplitudes of array channels for some scenarios are depicted in Figure S2 (color coded).

One limitation of our optimization is the consideration of the maximum current that the hardware can deliver (i_{max}). We conducted a study by varying the i_{max} value and repeating the optimization to determine the optimal value that produces the lowest E-field. The results of this study can be found in Figure S3. We used a maximum current value of 500 A for the presented scenarios. This maximum current value may vary based on the specific hardware setup. Because of the low inductance of the array channels, this value can be reached using low-level voltages. We also forced the adjacent channel currents not to have opposite directions, which may reduce the efficiency of the gradient array design.

Although our preliminary work did not address the array design manufacturability, a few key points should be highlighted. To implement the investigated design, 288 gradient power amplifiers are required. We are in the process of designing low-cost, custom-built power amplifiers, and the methodology for using these amplifiers to drive the gradient array design has been outlined in the

15222594, 2024, 3, Downloaded from https://onlinelibrary.wiley.com/doi/10.1002/mrm.30109 by Turkey Cochrane Evidence Aid, Wiley Online Library on [16/12/2024]. See the Terms and Conditions (https://onlinelibrary.wiley.com/terms-and-conditions) on Wiley Online Library for rules of use; OA articles are governed by the applicable Creative Commons License

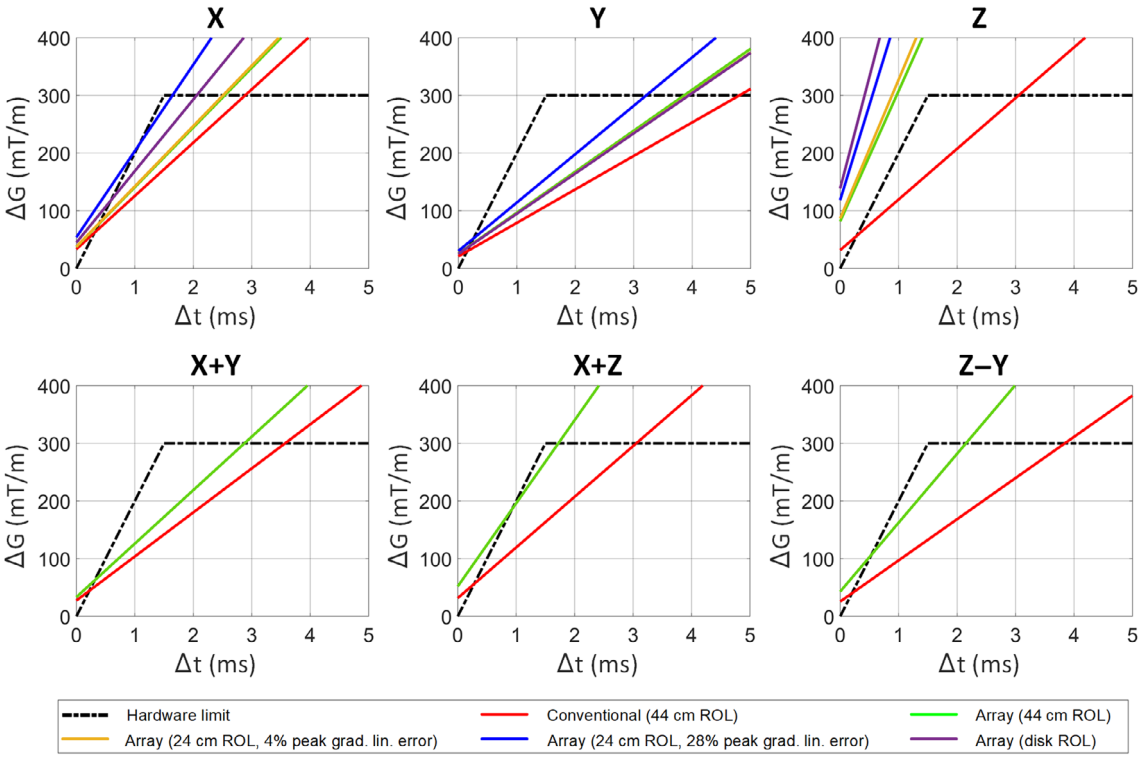

FIGURE 8 Calculated peripheral nerve stimulation (PNS) thresholds for the conventional coil and various array coil cases in six gradient directions. It is clear that the array design consistently yields higher PNS thresholds than the conventional design across all scenarios (ROL, region of linearity).

literature.[34,42] In this preliminary investigation, the DC resistance, wire spacing, connection cables, and heat dissipation in the windings have not been explored. The heating of the gradient coil (power deposition) is associated with the surface current density. Therefore, parameters such as peak current, wire diameter (cross-sectional area), and wire length can be optimized during the design phase of the array coils. Despite using a peak current of 500 A, which flowed through only a limited number of channels (as shown in Figure S2), the RMS currents remain comparable to those of conventional coils. Cooling systems similar to those used in existing setups[45] can be used to manage heat dissipation in gradient array coils.

Roemer and Rutt[30] explored the E-field limits for body-sized gradient coils optimized for a head ROL, suggesting the potential for generalized coil patterns that could approach the PNS performance of head coils. In our study, the X and Y gradient arrays did not achieve these lower E-fields when optimized on a 24-cm ROL. A likely explanation for this discrepancy is the fixed z-symmetric winding patterns of our coils (adopted from conventional coils), which are unable to generate a general current distribution. Exploring more general solutions would undoubtedly necessitate a more complex array design with overlapping wires or panels. Although such potential solutions should be explored in future research, they fall beyond the scope of our current work.

In our study, we used a simplified body model with uniform interior electrical properties. Therefore, the maximum induced E-field always occurs on the surface of the body model; however, this is not the case for heterogeneous body models. It is reasonable to expect that the performance of the gradient array coil in reducing E-fields would translate to similar benefits when applied to more realistic, heterogeneous body models. Using heterogeneous body models and considering the E-fields at precise nerve locations[26] would enhance the optimization performance. Targeting the optimization process to minimize the E-fields in regions critical for PNS is possible. However, this approach requires extensive knowledge of the body's nerve atlas.

The body position within the scanner greatly affects induced E-fields and, consequently, PNS thresholds.[31] Our simulations were conducted explicitly with the head placed at the iso-center. However, this can be broadened to accommodate various body positions by pre-calculating the E-field matrices for those positions and subsequently running the optimization. In such cases, the only required changes would be to the current combinations without physical hardware modifications. We anticipate achieving comparable E-field reduction performance with

15222594, 2024, 3, Downloaded from https://onlinelibrary.wiley.com/doi/10.1002/mrm.30109 by Turkey Cochrane Evidence Aid, Wiley Online Library on [16/12/2024]. See the Terms and Conditions (https://onlinelibrary.wiley.com/terms-and-conditions) on Wiley Online Library for rules of use; OA articles are governed by the applicable Creative Commons License

TABLE 1 $|E|_{max}$, ΔG_{min}, and SR_{min} values for the conventional and four array coil scenarios.

Gradient direction		$\|E\|_{max}$ (mV/m) per unit slew rate	ΔG_{min} (mT/m)	SR_{min} (T/m/s)
X	Conventional	23.81	33.26	92.4
	Array (44-cm ROL)	21.25	37.27	103.52
	Array (24-cm ROL, 4% peak lin. error)	21.03	37.66	104.61
	Array (24-cm ROL, 28% peak lin. error)	14.7	53.87	149.65
	Array (disk ROL)	17.73	44.67	124.08
Y	Conventional	37.89	20.9	58.06
	Array (44-cm ROL)	30.96	25.58	71.06
	Array (24-cm ROL, 4% peak lin. error)	31.49	25.15	69.86
	Array (24-cm ROL, 28% peak lin. error)	26.21	30.21	83.94
	Array (disk ROL)	31.55	25.1	69.73
Z	Conventional	25.02	31.65	87.92
	Array (44-cm ROL)	9.72	81.48	226.33
	Array (24-cm ROL, 4% peak lin. error)	9.14	86.65	240.7
	Array (24-cm ROL, 24% peak lin. error)	6.68	118.56	329.34
	Array (disk ROL)	5.7	138.94	385.96
X + Y	Conventional	28.81	27.49	76.36
	Array (44-cm ROL)	23.72	33.39	92.75
X + Z	Conventional	25.03	31.64	87.89
	Array (44-cm ROL)	15.26	51.9	144.16
Z–Y	Conventional	30.8	25.71	71.42
	Array (44-cm ROL)	18.41	43.02	119.5

Abbreviations: ROL, region of linearity; SR, slew rate.

the gradient array coil across different body positions, although this remains a topic for future exploration.

The optimization problem can be modified to maximize the gradient strength while ensuring that induced E-fields remain below certain thresholds. E-field thresholds can be set as nonlinear inequality constraints within the optimization framework. Alternatively, the gradient array coil can be optimized to deliver the highest possible gradient strength and slew rate while ensuring that PNS thresholds are not exceeded.

5 | CONCLUSION

We demonstrated the performance of the gradient array coil in reducing switched-gradient-induced E-fields and improving PNS thresholds. The gradient array technology provides a higher degree of freedom for field profiling, enabling the generation of desired gradients with flexible linearity across an adjustable ROL while minimizing the induced E-fields. We illustrated the array coil's ability to outperform a conventional coil in various imaging scenarios through extensive simulations and optimizations. Our study emphasized that gradient array design offers a promising pathway toward achieving high gradient performance, especially in scenarios in which linear magnetic fields are required within specific target regions. Additionally, the adaptability of the array design for different body positions within the scanner, even after coil construction, indicates its potential for personalized imaging.

ACKNOWLEDGMENTS

The authors gratefully acknowledge *Sim4Life* by ZMT (www.zurichmeditech.com) for providing an academic license. The authors thank Koray Ertan for providing the *MATLAB* code to generate the simplified body model. This study was partially supported by the Scientific and Technological Research Council of Turkey (Grant No. 121E128) and the Horizon Europe (Grant No. 101078393 "MRITwins").

15222594, 2024, 3, Downloaded from https://onlinelibrary.wiley.com/doi/10.1002/mrm.30109 by Turkey Cochrane Evidence Aid, Wiley Online Library on [16/12/2024]. See the Terms and Conditions (https://onlinelibrary.wiley.com/terms-and-conditions) on Wiley Online Library for rules of use; OA articles are governed by the applicable Creative Commons License

ORCID

Reza Babaloo https://orcid.org/0000-0002-2604-6491
Ergin Atalar https://orcid.org/0000-0002-6874-6103

REFERENCES

1. Setsompop K, Kimmlingen R, Eberlein E, et al. Pushing the limits of in vivo diffusion MRI for the human connectome project. *Neuroimage.* 2013;80:220-233.
2. Huang SY, Witzel T, Keil B, et al. Connectome 2.0: developing the next-generation ultra-high gradient strength human MRI scanner for bridging studies of the micro-, meso-and macro-connectome. *Neuroimage.* 2021;243:118530.
3. Fan Q, Eichner C, Afzali M, et al. Mapping the human connectome using diffusion MRI at 300 mT/m gradient strength: methodological advances and scientific impact. *Neuroimage.* 2022;254:118958.
4. Jones DK, Alexander DC, Bowtell R, et al. Microstructural imaging of the human brain with a 'super-scanner': 10 key advantages of ultra-strong gradients for diffusion MRI. *Neuroimage.* 2018;182:8-38.
5. Tang F, Liu F, Freschi F, et al. An improved asymmetric gradient coil design for high-resolution MRI head imaging. *Phys Med Biol.* 2016;61:8875-8889.
6. Turner R, Le Bihan D, Maier J, Vavrek R, Hedges LK, Pekar J. Echo-planar imaging of intravoxel incoherent motion. *Radiology*. 1990;177:407-414.
7. Wilm BJ, Hennel F, Roesler MB, Weiger M, Pruessmann KP. Minimizing the echo time in diffusion imaging using spiral readouts and a head gradient system. *Magn Reson Med.* 2020;84:3117-3127.
8. van Rijssel MJ, Zijlstra F, Seevinck PR, et al. Reducing distortions in echo-planar breast imaging at ultrahigh field with high-resolution off-resonance maps. *Magn Reson Med.* 2019;82:425-435.
9. Tan ET, Lee SK, Weavers PT, et al. High slew-rate head-only gradient for improving distortion in echo planar imaging: preliminary experience. *J Magn Reson Imaging.* 2016;44:653-664.
10. Ramos-Llordén G, Lobos RA, Kim TH, et al. High-fidelity, high-spatial-resolution diffusion magnetic resonance imaging of ex vivo whole human brain at ultra-high gradient strength with structured low-rank echo-planar imaging ghost correction. *NMR Biomed.* 2023;36:e4831.
11. Turner R. Gradient coil design: a review of methods. *Magn Reson Imaging.* 1993;11:903-920.
12. McNab JA, Edlow BL, Witzel T, et al. The Human Connectome Project and beyond: initial applications of 300 mT/m gradients. *Neuroimage.* 2013;80:234-245.
13. Reilly JP. Peripheral nerve stimulation by induced electric currents: exposure to time-varying magnetic fields. *Med Biol Eng Comput.* 1989;27:101-110.
14. Reilly JP. Maximum pulsed electromagnetic field limits based on peripheral nerve stimulation: application to IEEE/ANSI C95.1 electromagnetic field standards. *IEEE Trans Biomed Eng.* 1998;45:137-141.
15. Glover P. Interaction of MRI field gradients with the human body. *Phys Med Biol.* 2009;54:54-99.
16. Ham C, Engels J, Van de Wiel G, Machielsen A. Peripheral nerve stimulation during MRI: effects of high gradient amplitudes and switching rates. *J Magn Reson Imaging.* 1997;7:933-937.
17. Zhang B, Yen YF, Chronik BA, McKinnon GC, Schaefer DJ, Rutt BK. Peripheral nerve stimulation properties of head and body gradient coils of various sizes. *Magn Reson Med.* 2003;50:50-58.
18. Kimmlingen R, Gebhardt M, Schuster J, Brand M, Schmitt F, Haase A. Gradient system providing continuously variable field characteristics. *Magn Reson Med.* 2002;47:800-808.
19. Goodrich KC, Hadley JR, Kim SE, et al. Peripheral nerve stimulation measures in a composite gradient system. *Concepts Magn Reson B Magn Reson Eng.* 2014;44:66-74.
20. Foo TK, Laskaris E, Vermilyea M, et al. Lightweight, compact, and high-performance 3 T MR system for imaging the brain and extremities. *Magn Reson Med.* 2018;80:2232-2245.
21. Foo TK, Tan ET, Vermilyea ME, et al. Highly efficient head-only magnetic field insert gradient coil for achieving simultaneous high gradient amplitude and slew rate at 3.0 T (MAGNUS) for brain microstructure imaging. *Magn Reson Med.* 2020;83:2356-2369.
22. Davids M, Dietz P, Ruyters G, et al. Peripheral nerve stimulation informed design of a high-performance asymmetric head gradient coil. *Magn Reson Med.* 2023;90:784-801.
23. Den Boer JA, Bourland JD, Nyenhuis JA, et al. Comparison of the threshold for peripheral nerve stimulation during gradient switching in whole body MR systems. *J Magn Reson Imaging.* 2002;15:520-525.
24. Irnich W, Hebrank FX. Stimulation threshold comparison of time-varying magnetic pulses with different waveforms. *J Magn Reson Imaging.* 2009;29:229-236.
25. Feldman RE, Hardy CJ, Aksel B, Schenck J, Chronik BA. Experimental determination of human peripheral nerve stimulation thresholds in a 3-axis planar gradient system. *Magn Reson Med.* 2009;62:763-770.
26. Davids M, Guérin B, Klein V, Wald LL. Optimization of MRI gradient coils with explicit peripheral nerve stimulation constraints. *IEEE Trans Med Imaging.* 2020;40:129-142.
27. Davids M, Guérin B, Malzacher M, Schad LR, Wald LL. Predicting magnetostimulation thresholds in the peripheral nervous system using realistic body models. *Sci Rep*. 2017;7:5316.
28. Davids M, Guérin B, Vom Endt A, Schad LR, Wald LL. Prediction of peripheral nerve stimulation thresholds of MRI gradient coils using coupled electromagnetic and neurodynamic simulations. *Magn Reson Med.* 2019;81:686-701.
29. Roemer PB, Wade T, Alejski A, McKenzie CA, Rutt BK. Electric field calculation and peripheral nerve stimulation prediction for head and body gradient coils. *Magn Reson Med.* 2021;86:2301-2315.
30. Roemer PB, Rutt BK. Minimum electric-field gradient coil design: theoretical limits and practical guidelines. *Magn Reson Med.* 2021;86:569-580.
31. Davids M, Guerin B, Wald LL. A Huygens' surface approach to rapid characterization of peripheral nerve stimulation. *Magn Reson Med.* 2022;87:377-393.
32. Harvey PR, Katznelson E. Modular gradient coil: a new concept in high-performance whole-body gradient coil design. *Magn Reson Med.* 1999;42:561-570.
33. Hidalgo-Tobon SS, Bencsik M, Bowtell R. Reducing peripheral nerve stimulation due to gradient switching using an additional uniform field coil. *Magn Reson Med.* 2011;66:1498-1509.
34. Ertan K, Taraghinia S, Atalar E. Driving mutually coupled gradient array coils in magnetic resonance imaging. *Magn Reson Med.* 2019;82:1187-1198.

15222594, 2024, 3, Downloaded from https://onlinelibrary.wiley.com/doi/10.1002/mrm.30109 by Turkey Cochrane Evidence Aid, Wiley Online Library on [16/12/2024]. See the Terms and Conditions (https://onlinelibrary.wiley.com/terms-and-conditions) on Wiley Online Library for rules of use; OA articles are governed by the applicable Creative Commons License

35. Takrimi M, Atalar E. A z-gradient array coil with a dedicated active-shielded array coil for MRI. *Magn Reson Med.* 2022;88:2718-2731.
36. Smith E, Freschi F, Repetto M, Crozier S. The coil array method for creating a dynamic imaging volume. *Magn Reson Med.* 2017;78:784-793.
37. Juchem C, Nahhass OM, Nixon TW, de Graaf RA. Multi-slice MRI with the dynamic multi-coil technique. *NMR Biomed.* 2015;28:1526-1534.
38. Jia F, Littin S, Layton KJ, Kroboth S, Yu H, Zaitsev M. Design of a shielded coil element of a matrix gradient coil. *J Magn Reson Imaging.* 2017;281:217-228.
39. Littin S, Jia F, Layton KJ, et al. Development and implementation of an 84-channel matrix gradient coil. *Magn Reson Med.* 2018;79:1181-1191.
40. Babaloo R, Takrimi M, Atalar E. Increasing peripheral nerve stimulation thresholds using gradient array coils. *Proceedings of Joint Annual Meeting of ISMRM-ESMRMB*; 2022;580.
41. Babaloo R, Takrimi M, Atalar E. Minimum electric field gradient array body coil with adjustable regions of linearity. *Proceedings of the 32nd Annual Meeting of ISMRM*; 2023;599.
42. Babaloo R, Atalar E. Nonlinear droop compensation for current waveforms in MRI gradient systems. *Magn Reson Med.* 2022;88:973-985.
43. Takrimi M, Atalar E. A novel method to estimate and control the eddy power loss within the cryostat: a co-simulation approach to tune Z-gradient Array coil. *Proceedings of the 32nd Annual Meeting of ISMRM*; 2023;4573.
44. IEC. IEC standard 60601-2-33: medical electrical equipment—Part 2-33: particular requirements for the basic safety and essential performance of magnetic resonance equipment for medical diagnosis. 2015.
45. Theilenberg S, Shang Y, Ghazouani J, et al. Design and realization of a multi-coil array for B0 field control in a compact 1.5 T head-only MRI scanner. *Magn Reson Med.* 2023;90:1228-1241.

SUPPORTING INFORMATION

Additional supporting information may be found in the online version of the article at the publisher's website.

FIGURE S1. The left column illustrates the B-field profiles of conventional gradient coils. The middle column shows the B-fields of the array coil with a 44-cm region of linearity (ROL) (same as the conventional coil). However, direct comparisons of magnetic-field values between the array and conventional coils are not appropriate due to the optimization relying on the gradient of these fields. Thus, the magnetic-field values might vary compared with the conventional coil, particularly evident in the Z gradient profile. The right column displays the B-fields of the array coil when generating the target gradient within a 24-cm ROL with a 28% peak linearity error. All profiles are shown in the center plane.

Figure S2. The color-coded current amplitudes. The first row illustrates the currents of array channels for the X coil in three scenarios (44-cm ROL, 24-cm ROL with 28% peak linearity error, and the disk ROL at $z = 0$). The second row depicts the currents for the Z coil. Despite the winding patterns having z-symmetry, the resulting optimized currents can be nonsymmetric.

Figure S3. Maximum E-field magnitude corresponds to i_{max} for the first scenario (44-cm ROL). The red stars represent the peak E-fields induced by the conventional coils, in which the driving currents for the X, Y, and Z gradients are 240 A, 252 A, and 138 A, respectively. Each green diamond represents a solution for the optimization of the array coil. As shown in the plots, by increasing the i_{max} up to 500 A, it is possible to reduce the E-fields. However, further reduction in the E-fields is not achieved beyond this point. Although the maximum allowable current of 500 A is used in this study, the RMS of currents required to generate the target gradient by the array coil is as follows: 285 A for the X gradient, 334 A for the Y gradient, and 149 A for the Z gradient.

How to cite this article: Babaloo R, Atalar E. Minimizing electric fields and increasing peripheral nerve stimulation thresholds using a body gradient array coil. *Magn Reson Med*. 2024;92:1290-1305. doi: 10.1002/mrm.30109

15222594, 2024, 3, Downloaded from https://onlinelibrary.wiley.com/doi/10.1002/mrm.30109 by Turkey Cochrane Evidence Aid, Wiley Online Library on [16/12/2024]. See the Terms and Conditions (https://onlinelibrary.wiley.com/terms-and-conditions) on Wiley Online Library for rules of use; OA articles are governed by the applicable Creative Commons License